

On the Chemistry and Physical Properties of Flux and Floating Zone Grown SmB₆ Single Crystals

W. A. Phelan,^{1,2,3*} S. M. Koohpayeh,² P. Cottingham,^{1,2,3} J. A. Tutmaher,^{1,2,3} J. C. Leiner,⁴ M. D. Lumsden,⁴ C. M. Lavelle,⁵ X. P. Wang,⁶ C. Hoffmann,⁶ M. A. Siegler,¹ and T. M. McQueen^{1,2,3*}

¹*Department of Chemistry, Johns Hopkins University, Baltimore, MD 21218, USA*

²*Institute for Quantum Matter, Department of Physics and Astronomy, Johns Hopkins University, Baltimore, MD 21218, USA*

³*Department of Materials Science and Engineering, Johns Hopkins University, Baltimore, MD 21218, USA*

⁴*Quantum Condensed Matter Division, Oak Ridge National Laboratory, Oak Ridge, TN 37831, USA*

⁵*Applied Nuclear Physics Group, Johns Hopkins University, Applied Physics Laboratory, Laurel, MD, 20723, USA*

⁶*Chemical and Engineering Materials Division, Neutron Sciences Directorate, Oak Ridge National Laboratory, Oak Ridge, TN 37831, USA*

*wphelan2@pha.jhu.edu and mcqueen@jhu.edu

Abstract

Recent theoretical and experimental findings suggest that the long-known but not well understood low temperature resistance plateau of SmB₆ may originate from protected surface states arising from a topologically non-trivial bulk band structure having strong Kondo hybridization. Yet other studies have ascribed this feature to impurity phases, sample vacancies, and surface reconstructions. Given the typical methods used to prepare SmB₆ single crystals, the flux and floating zone procedures, these ascriptions should not be taken lightly. Here, we demonstrate how compositional variations and observable amounts of impurity phases in SmB₆ crystals grown by floating zone and flux affect the physical properties. From neutron diffraction and X-ray computed tomography experiments, we observe that a ¹⁵⁴Sm¹¹B₆ crystal prepared using aluminum flux contains co-crystallized, epitaxial aluminum. A large, nearly stoichiometric crystal of SmB₆ was successfully grown using the float-zone technique; upon continuing the zone melting, samarium vacancies are introduced. These samarium vacancies drastically alter the resistance and plateauing magnitude of the low temperature resistance compared to stoichiometric SmB₆. These results highlight that small presences of impurity phases and compositional variations must be considered when collecting and analyzing physical property data of SmB₆. Finally, a more accurate samarium-154 coherent neutron scattering length value, 8.9(1) fm, is reported.

Introduction

The lanthanide hexaborides, LnB_6 ($Ln = La-Nd, Sm, \text{ and } Eu-Ho, Yb, \text{ and } Y$), comprise a fascinating class of materials which crystallize with a primitive cubic structure ($a \sim 4.1 \text{ \AA}$, $V \sim 70 \text{ \AA}^3$, $Z = 1$, and $SG = Pm-3m$).¹ In the case of $Ln = Sm$, many theoretical and experimental studies of SmB_6 have been performed for more than four decades and have focused on its samarium ion mixed valence nature (Sm^{+2} and Sm^{+3}), Kondo insulating behavior, and the mysterious plateau commonly observed in the low temperature regime of many temperature dependent resistance datasets.^{2,3} More recently, theoretical and experimental studies have focused on the possibility that Kondo insulating SmB_6 harbors non-trivial topological protected surface states, which might provide an explanation for the low temperature resistance plateau.⁴⁻²³ However, previous literature claims that this remnant metallic feature results from combinations of impurity phases and compositional variations.^{24,25}

To determine the possible contributions of impurity phases and compositional variations to the low temperature resistance behavior, a central need is high quality single crystals of SmB_6 with precisely defined and controlled stoichiometry. The main procedures used to synthesize single crystals of SmB_6 are the floating zone (FZ) and flux growth (FG) methods. In general, the FG technique is used to grow crystals below their melting temperature, and as a result, high temperature decomposition can be prevented. However, the major disadvantages of this technique can include crystal products that are small in size, the presence of flux inclusions within the crystal, contamination from the melt container, and possible inhomogeneities in the crystal due to inconsistent linear growth rates of different facets that develop during growth. In contrast to the FG technique, the use of the crucible-and flux-less FZ technique circumvents the problem of the incorporation of impurities from the crucible and flux materials; further, the grown crystals are quite large and can be manipulated easily. However, preparing single crystals *via* this technique, which is widely used for the crystal growth of the congruently or near congruently melting compounds, can be more complicated for the materials with instabilities near their melting temperature.²⁶

Here, we report the results of a comparative study of *FZ* and *FG* single crystals of SmB_6 . We find large systematic changes in the occurrence of the low-temperature resistance plateau with small but systematic changes in the lattice parameters of *FZ* prepared SmB_6 along the length of a large single crystal, showing that small changes in composition have large effects on this and other physical properties of SmB_6 . Further, single crystal neutron diffraction studies of a doubly isotope enriched *FG* $^{154}\text{Sm}^{11}\text{B}_6$ single crystal revealed the presence of epitaxially oriented, co-crystallized aluminum. These results show that metallic aluminum incorporated into *FG* crystals of SmB_6 will have an effect on the physical properties of crystals prepared using this method. Finally, using the neutron diffraction experiments, we have determined a more accurate coherent neutron scattering length value of 8.9(1) fm for samarium-154.

Results and Discussion

Chemistry and Physical Properties. As mentioned above, the *FG* procedure is a common method used to grow LnB_6 single crystals. A typical photograph SmB_6 crystal grown using the *FG* procedure is shown in Figure 1a. The crystal has several facets and is of the appropriate size for diffraction experiments and physical properties measurements. Under magnification, portions of surface of this crystal are coated with a lustrous, metallic substance (likely residual aluminum flux), which is typically etched away prior to physical property measurements.

Using single crystal neutron diffraction, which effectively probes the entire sample volume due to the penetrating power of neutrons, we find the residual aluminum is not confined to the surfaces of this doubly isotope enriched crystal, which was grown using samarium-154 and boron-11 (The least neutron absorbing, stable isotopes of samarium and boron.). Figure 2a shows a neutron precession image along the $(00l)$ and $(h00)$ directions. A set of companion peaks (white arrow) accompany the main SmB_6 Bragg reflections. To identify this satellite crystallite, a powder-like neutron diffraction histogram was obtained from the radial integration of the single crystal neutron diffraction data, Figure 2b. The asterisk denotes the reflections from the secondary phase. We identify it as aluminum metal for three reasons: first, the lattice parameter ($a = 4.053(3) \text{ \AA}$) is within 0.09-0.3% of the literature values for aluminum; second, the systematic absences are consistent with the $Fm-3m$ space group of Al; and third, there are no other known

compounds that can explain these diffraction peaks and the observed lattice constant containing some combination of Ln , B, C, V, and Al ($Ln = \text{La-Nd}$ and Sm-Lu). An aluminum/ SmB_6 co-Rietveld refinement to the powder averaged data showed the ratio of aluminum: SmB_6 was $\sim 4 \text{ wt\%}:96 \text{ wt\%}$ or $\sim 25 \text{ mol\%}:75 \text{ mol\%}$. Such a significant amount of well-ordered aluminum cannot originate solely from a surface coating, and instead demonstrates that aluminum inclusions are present within this SmB_6 FG crystal. This is not surprising given the similar crystal structures of SmB_6 and aluminum (cubic crystal symmetry with the a -lattice parameters for both being $\sim 4.1 \text{ \AA}$), the large excess of aluminum flux required for growths given the solubility of boron under typical FG conditions, and the previous reports of metallic inclusions during FG crystal polishing.^{24,27}

To check the validity of the neutron experiments and data analysis, X-ray computed tomography (CT) volumetric data of the FG $^{154}\text{Sm}^{11}\text{B}_6$ crystal were obtained using this crystal. A resulting image of the 3D reconstruction is shown above the precession image in Figure 2a, and a movie generated from the reconstruction of the frames has been added to the Supplementary Information (Figure S1.). Regions composed of materials with high Z (atomic number) and/or high number density will attenuate the X-ray beam more strongly than lower Z , low density regions. Clearly, this crystal is comprised of two materials: one with a high average Z (atomic number, dark contrast), and a second with low, but non-negligible, average Z (light contrast). This is exactly what would be expected for a SmB_6 crystal with Al inclusions: the SmB_6 corresponds to the high Z regions, and the Al the low Z regions. Several features of the aluminum inclusions are evident: they are not confined to the surface, but instead are included deep within the crystal, have well-defined facets oriented non-randomly with respect to the host, and are present in an amount consistent with aluminum/ SmB_6 co-Rietveld refinements to the neutron data.

A surprising finding from our neutron and X-ray CT data is that the aluminum inclusions are not randomly oriented, but instead maintain a nearly epitaxial registry with the hexaboride, and have non-negligible size. These inclusions, which will not necessarily affect the electrical transport at low temperature (plateau region) as they are embedded in a host insulating material, would provide an

alternate explanation for the origin of high frequency and light mass quantum oscillations observed in torque magnetometry experiments on *FG* SmB₆ samples. However, given their size, variability in the number of such inclusions is likely and should be checked on a crystal by crystal basis.

In order to avoid flux inclusions and grow a larger, more homogeneous and higher purity crystal of SmB₆, which is reported to be a congruently melting compound, the *FZ* technique was successfully utilized to produce the SmB₆ single crystal shown in Figure 1b. This crystal, measuring roughly 8 cm in length, is considerably larger than SmB₆ single crystals that can be prepared using *FG*. Similar to *FG* SmB₆, there are also composition variations in the *FZ* crystal.

To understand the origin of the composition variation, four individual cuts were taken from the *FZ* grown crystal (Figure 3b Inset), and a portion of each individual cut was used for synchrotron powder X-ray diffraction while another portion was used for physical property measurements followed by trace elemental analysis. The resulting synchrotron powder X-ray diffraction data and fit for cut 1 is shown in Figure 3a; similar quality fits are obtained for cuts 2-4 (Figure S2 in the Supplementary Information). Final parameters for all refinements are given in Table 1. There is a systematic change in lattice parameters across the cuts. Going from cut 1 to cut 3, the lattice parameters decrease, while the lattice parameter for cut 4 is similar to cut 3. This is shown graphically in Figure 3b and Figure S4. The refined *a*-lattice parameter value for the polycrystalline feed rod, as confirmed by powder X-ray diffraction, is shown as a blue dashed line, which lies between the start (cut 1) and end (cut 4) of the grown crystal. This is consistent with the temperature-composition phase diagram for the Sm-B system which indicates that by fully melting a feed rod with the composition either near to the stoichiometric ratio (Sm/B : 1/6) or over the range of Sm to B atomic percent ratios from ~14.3% Sm-85.7% B (Sm/B : 1/6) to ~9.0% Sm-91.0% B (Sm/B : 1/10), the first solidified crystal would have the highest possible Sm to B ratio within the SmB₆ crystal structure (at ~14.3 at%Sm-85.7at%B).²⁸ This explains how a larger lattice parameter of 4.1343 Å obtained for the initially growing crystal occurs with the use of a polycrystalline feed rod with a slightly smaller lattice parameter of 4.1333 Å.

Attempts to directly identify the precise origin of the compositional change from Rietveld refinements or trace elemental analysis were unsuccessful. When the boron and samarium occupancy parameters for all cuts were allowed to individually float during separate Rietveld refinement cycles, no significant deviation from unity was noticed for either on any dataset. As such, for all final refinements the occupancy parameters for boron and samarium were fixed at unity. Trace elemental analysis via glow discharge mass spectrometry (GDMS) also showed no systematic trends in total, rare earth, or transition metal impurity levels as a function of rod length, Figure S6 and Table S4.

Nonetheless, the lattice parameters listed in Table 1, combined with previous robust elemental analyses, do provide insight into the composition differences between the different *FZ* cuts. The lattice parameter for cut 1 is in excellent agreement with the lattice parameter ($a = 4.1342(5) \text{ \AA}$) determined for stoichiometric SmB_6 as reported by Tarascon *et. al.*,²⁹ and close to Paderno *et. al.*'s most stoichiometric sample of SmB_6 ($a = 4.13334(2) \text{ \AA}$).³⁰ The reduction of the lattice parameter in subsequent cuts is consistent with the formation of samarium vacancies, based on Paderno *et. al.*'s careful chemical analyses which found that the a -lattice parameter decreases as the samarium content decreases. While the variation between cuts 1 to 4 is small, less than 1% or $\text{Sm}_{1-x}\text{B}_6$ ($x = 0.01$), based on the a -lattice parameter of $4.1317(2) \text{ \AA}$ for $\text{Sm}_{0.97}\text{B}_6$ and assuming Vegard's law applies, we have evidence that this compositional variation is due to vaporization during growth. During each growth, we observe vaporization of a small (~1%) amount of the rod material. Using laboratory powder X-ray diffraction, the vaporized powder was confirmed to be a multiphase mixture of SmB_6 and SmB_4 , i.e. samarium rich compared to the feed rod, implying a relative loss of samarium in the growing crystal (Figure S3 in the Supplementary Information). While this loss of material could be due to stoichiometric SmB_6 being an incongruent melter, a more likely explanation is a slight non-stoichiometry in the feed rods themselves: the lattice parameter for the polycrystalline feed rod starting material is slightly nonstoichiometric relative to the most stoichiometric portion of our grown *FZ* single crystal (cut 1). These results, however, are in contrast to a recent SmB_6 thin-film study, where the authors found that the lattice parameter increased with increasing samarium vacancy content. This result is consistent with lattice mismatch effects on the MgO

substrate, where the higher samarium vacancy nanocrystal films become strained, and as more samarium is added the lattice mismatch is reduced, and thus the size of the lattice constant decreases.³¹

The structural parameters can also be used to independently determine the samarium valence. The structure of SmB_6 , shown in Figure 4a, adopts the CaB_6 structure-type, or more descriptively is analogous to CsCl where the Sm atoms occupy the vertices of a cube and the B_6 octahedra lie in the center of the unit cell. An additional structural feature shown in Figure 4a is the bonding between B_6 octahedra (inter), which is shorter in distance compared to the boron-boron bonds forming the B_6 octahedra (intra), that forms a three dimensional interconnected cage structure. The intra-octahedral boron-boron bond distances normalized by the inter-octahedral boron distances (Intra B-B/Inter B-B) for selected hexaborides versus different charges of the B_6 cluster (B_6^x ; $x = -4, -3, \text{ and } -2$) are plotted in Figure 4b. Also shown are the Intra B-B/Inter B-B values for all SmB_6 *FZ* cuts and *FG* SmB_6 versus charge of the B_6 cluster for all charges (dashed line). Relative to the -4 (ThB_6)³² and -2 (CaB_6 , SrB_6 , BaB_6 , and EuB_6)³³⁻³⁵ charges, the charge on the B_6 cluster for all SmB_6 samples appears to most closely resemble -3 (NdB_6 and LaB_6)^{35,36}. However, the dashed line falls slightly below the Intra B-B/Inter B-B values for NdB_6 and LaB_6 ,^{34,36} and this is consistent with a partial mixed valency. Applying a lever-type rule, an estimate of the $\text{Sm}^{+3}:\text{Sm}^{+2}$ ratio for all samples was determined to be $\sim 80\%:20\%$. Given that the Intra B-B/Inter B-B values for all SmB_6 samples lie on the dashed line in Figure 4b, this suggests that while the composition changes along the *FZ* crystal have noticeable effects on the lattice parameters, the overall samarium vacancies and valence are not drastically altered along the length of the crystal (this is not unexpected as the samarium content is changing by $<1\%$). It is interesting to note that these data, which are consistent with a $\text{Sm}^{+2.80}\text{B}_6$ scenario, are not necessarily in quantitative agreement with the findings of other experiments like X-ray absorption spectroscopy (XAS) where those data and analysis show that bulk SmB_6 has a mixed valence nature closer to $\text{Sm}^{+2.60}\text{B}_6$.^{29,37} The most plausible explanation for this difference, if real, is that in addition to formal changes in the oxidation states, there are configurational changes that occur on samarium without a change of formal oxidation state.

To see how the changes in composition along the *FZ* crystal affect the physical properties of SmB_6 , temperature dependent resistance data were collected for each *FZ* cut. The 300 K normalized resistance data for all cuts are plotted from $T = 2 - 300$ K in Figure 5. At higher temperatures the data from all cuts closely resemble the resistance data reported for a majority of SmB_6 samples. That is, the resistances are roughly temperature independent from 300 K to 100 K, increase dramatically below 40 K, and have some degree of plateauing below ~ 10 K. We find systematic variations in the low temperature behavior with changing samarium vacancy concentration. The low temperature remnant metallicity decreases from cut 1 to cut 3 along with the overall normalized resistance values, while the features for cuts 3 and 4 are seemingly identical. The degree of reproducibility of these resistance curves is highlighted in Figure S5. This figure shows a second set of measurements where new contacts replaced the old contacts of the original cuts 1-3 (open colored circles) and resistances were measured using a new cut between the location of the original cut1 and cut 2 and a new cut beyond the location of the original cut 4 (filled gray squares). We have previously shown that electron doping SmB_6 *via* the replacement of carbon for boron in the boron sub-lattice can induce a low temperature resistance plateau.²² Samarium vacancies will introduce holes, rather than electrons, and from our previously proposed density of states model, this is expected to reduce the degree of resistance plateauing in SmB_6 .²² Taken together, these observations suggest that the composition along the *FZ* crystals is being changed systematically, and that these small changes in compositions produce noticeable changes in physical properties. These results and our previous SmB_6 dopant study highlight the utility of the *FZ* technique to systematically control crystal stoichiometry in SmB_6 .²²

¹⁵⁴Sm Neutron Scattering Length Determination. The previously best determined coherent neutron scattering length value (8.0(1.0) fm) for samarium-154 ($b_{154\text{Sm}}$) has a large uncertainty that makes it unsuitable for detailed refinements of single crystal neutron diffraction data, and thus for determination of any Sm:B non-stoichiometry.³⁸ We thus performed the necessary experiments to provide a refined number with an order of magnitude reduced uncertainty.

Two small crystal pieces were removed from the doubly isotope enriched $^{154}\text{Sm}^{11}\text{B}_6$ *FG* single crystal shown in Figure 1a. The first piece was used to determine the various samarium and boron isotope ratios *via* ICP-MS, while the second piece was used to collect a large and highly redundant single crystal X-ray diffraction dataset (see SI). Refinements to this dataset returned the best goodness-of-fit statistics when the composition of this crystal was set to $\text{SmB}_{5.88}$ and all other parameters were allowed to float (Table S1 and S2). Using this composition, the known coherent scattering lengths for 10-boron (^{10}B) and 11-boron (^{11}B),³⁸ and determining the overall coherent neutron scattering length for boron in this crystal *via* $b_{\text{B}} = w_1^{10}\text{B} + w_2^{11}\text{B} = 6.4(1)$ fm where w_1 and w_2 were determined from the ICP-MS data; an overall coherent neutron scattering length of 8.85 fm was determined for the combination of samarium isotopes ($b_{x\text{Sm}}$) in the doubly isotope enriched single crystal through a series of refinements to the $T = 295$ K neutron diffraction data. When the errors based on the X-ray refinements and compositions for $b_{x\text{Sm}}$ and b_{B} were taken into account, respectively, the overall coherent scattering length value is found to equal 8.9(1) fm. Finally, after setting this value equal to the weighted values (Again, these values were determined from the ICP-MS data.) of the known coherent scattering lengths of the samarium isotopes present in this crystal (^{144}Sm , ^{147}Sm , ^{148}Sm , ^{149}Sm , ^{150}Sm , and ^{152}Sm),³⁸ a new value equal to 8.9(1) fm was determined for ^{154}Sm (Table S3).

Once the b_{B} and $b_{x\text{Sm}}$ were set to be 6.4(1) fm and 8.9(1) fm, respectively, refinements to the $T = 90$ K and 295 K neutron data were performed. The crystallographic parameters and refinement statistics for both temperatures are provided in Table 2, and the atomic fractional coordinates, site occupancies, and ADPs are given in Table 3. During separate refinements the samarium and boron occupancy parameters were allowed to float. In all refinements, the resulting occupancies were found to be within 3σ of unity, thus, the information in Tables 3 and 4 reflect refinements where the occupancies have been set to unity.

Conclusions

Structural data for *FG* and *FZ* single crystals of SmB_6 have been compared. Observable amounts of impurity phases and compositional variations can have large effects on the physical properties of SmB_6

crystals prepared using *FG* and *FZ* procedures, respectively. In particular, epitaxially oriented aluminum inclusions are found in *FG* crystal and samarium vacancies found in *FZ* crystal. Further, the boron-boron bond distances determined from our X-ray and neutron refinements are consistent with mixed valency with a formula close to $\text{Sm}^{+2.80}\text{B}_6$. The changes in boron-boron bond distances for SmB_6 and other hexaborides determined using temperature dependent X-ray and neutron scattering data would be interesting to study in order to see if changes in the charge transfer to the B_6 cage for SmB_6 occur relative to other hexaborides. Finally, we have determined that the coherent neutron scattering length for samarium-154 equals 8.9(1) fm, a value an order of magnitude more accurate than previously known.

Methods

Synthesis. A single crystal of SmB_6 with approximate dimensions of 80 mm in length and 6 mm diameter was prepared from polycrystalline rods of SmB_6 (Testbourne Ltd, 99.9%) using a four-mirror optical floating zone furnace (Crystal Systems Inc FZ-T-12000-X-VPO-PC) with 4×3 kW Xe lamps as the heating source. The crystal growth was performed by melting the polycrystalline feed rod onto a seed rod, then running the molten zone in an upward direction along the feed rod (defining the growth direction) at a zoning rate of 10 mm/h, under flowing ultra-high purity argon at a pressure of 2 bar with a flow rate of 2 L/min, and the rotation rate of 10 rpm for the growing crystal. Only one zone pass was required for the growth. Slices of the crystal were cut close to the [100] orientation using a diamond saw.

The *FG* single crystal of doubly isotope enriched SmB_6 ($^{154}\text{Sm}^{11}\text{B}_6$), needed for the single-crystal neutron diffraction experiments as naturally occurring samarium and boron are largely comprised of isotopes that absorb neutrons, was provided by Oak Ridge National Laboratory (ORNL).

Powder X-ray Diffraction. Slices cut from a large *FZ* grown SmB_6 single crystal were ground using a stainless steel mortar and pestle. A small amount of a powdered silicon standard ($\text{SG} = Fd-3m$ and $a = 5.43102 \text{ \AA}$) was added to the resulting SmB_6 powder for each cut. To acquire a high intensity-high resolution powder X-ray diffraction dataset, synchrotron powder X-ray diffraction data were obtained at $T = 295 \text{ K}$ using the 11-BM beam line ($\lambda = 0.4136820 \text{ \AA}$) at the Advanced Photon Source within Argonne National Laboratory.³⁹ The data points were collected over a 2θ range $0.5^\circ - 50^\circ$ with a

step size of 0.001° and step time of 0.1 seconds. Le Bail fits and Rietveld refinements were conducted using the GSAS/EXPGUI software to optimize the lattice/instrumental (GU, GV, and GW) and structure parameters for the SmB_6 models, respectively.^{40,41} The crystallographic parameters and refinement statistics for all cuts are provided in Table 1.

All laboratory powder X-ray diffraction patterns were collected using $\text{Cu } K\alpha$ radiation on a Bruker D8 Focus diffractometer with a LynxEye detector. The same silicon standard described above (SG = $Fd-3m$ and $a = 5.43102 \text{ \AA}$) was mixed in with powder from the polycrystalline rods of SmB_6 purchased from Testbourne Ltd. Rietveld refinements were performed in TOPAS (Bruker AXS) to determine a lattice parameter of $a = 4.133387(2) \text{ \AA}$.

Single Crystal X-ray Diffraction. A small piece of a doubly isotope enriched crystal of $^{154}\text{Sm}^{11}\text{B}_6$ was mounted onto a fiber using epoxy. All reflection intensities were measured under ambient conditions using a SuperNova diffractometer (equipped with an Atlas detector) employing $\text{Mo } K\alpha$ radiation ($\lambda = 0.71073 \text{ \AA}$) under the CrysAlisPro software package (version 1.171.36.28, Agilent Technologies, 2012). Unit cell indexing and data reductions were performed using the CrysAlisPro software. The generation of the initial models and structure refinements were performed using SIR97 and SHELXL-2013, respectively.^{42,43} The selection of the $Pm-3m$ was based on the observed Laue symmetry and the systematic absences. After the refinement of the atomic positions, the collected data were corrected for absorption using an analytic correction.⁴⁴ During the final stages of refinements the atomic displacement parameters (ADPs) were refined as anisotropic and weighting schemes were applied. The crystallographic parameters and refinement statistics are provided in Table S1, and the atomic fractional coordinates, site occupancies, and ADPs are given in Table S2.

Single Crystal Neutron Diffraction. Single crystal neutron diffraction experiments were performed using the TOPAZ beam line at the Spallation Neutron Source at ORNL using a doubly isotope enriched crystal of $^{154}\text{Sm}^{11}\text{B}_6$. A FG crystal with dimensions of $1.05 \times 1.10 \times 1.55 \text{ mm}$ was mounted onto a Kapton covered vanadium post with Loctite instant adhesive (495) and positioned onto the goniometer. Data collections were performed at $T = 90 \text{ K}$ and 295 K in wavelength-resolved time-of-flight (TOF)

Laue mode using neutrons with a wavelength range of $\lambda = 0.6\text{-}3.5 \text{ \AA}$. To ensure good coverage and redundancy for each data collection, data were collected with 13 detectors and using 13 to 15 crystal orientations, which were selected by evaluation with CrystalPlan software,⁴⁵ with collection times of approximately 3 hours per orientation. The integrated raw Bragg intensities were obtained using the 3-D ellipsoidal Q-space integration method in Mantid.⁴⁶ Data were corrected for background and detector efficiency. Data reduction including, Lorentz, neutron TOF spectrum, and absorption corrections was carried out with the local ANVRED2.⁴⁷ The reduced data were saved in SHELX HKLF2 format in which the wavelength is recorded separately for each individual reflection, and the reduced data were not merged as a consequence of the saved format. The crystallographic parameters and refinement statistics for both temperatures are provided in Table 2, and the atomic fractional coordinates, site occupancies, and ADPs are given in Table 3

Mass Spectrometry. Inductively coupled plasma mass spectrometry (ICP-MS) experiments and data analysis were performed at the Water Quality Center at Trent University in Ontario, Canada to determine the concentrations of the differing samarium and boron isotopes in the *FG* doubly isotope enriched $^{154}\text{Sm}^{11}\text{B}_6$ single crystal (See Table S3).

Glow discharge mass spectrometry (GDMS) and data analysis were performed by Evans Analytical Group to determine the concentrations of elements in the starting material, cut 1, cut 2, and cut 3 (See Table S4.).

X-ray computed tomography. The X-ray computed tomography (CT) data was collected on the $^{154}\text{Sm}^{11}\text{B}_6$ flux grown single crystal using a Bruker Skyscan 1172G. The source was set to 100kV/57 μA . Frames were collected in 0.5 degree steps using a 500 μm Al + Cu filter and SHT 11 Mp camera, with averaging of 100, 1.48 s exposures per angle and median filtering for 2.21 μm nominal resolution. Reconstruction was performed using the associated software. The final images were generated in attenuation mode, with contrast adjusted to visualize low Z inclusions.

Physical Properties. Temperature dependent resistance data were collected using the resistivity option of a 9-Tesla Quantum Design Physical Property Measurement System (PPMS). The

measurements were performed using a standard four-probe method, where platinum leads were mounted in a linear configuration onto the crystals using silver epoxy. All crystals were bar shaped and had roughly the same geometric factors (length ~ 1.00 mm and cross-sectional area ~ 1.25 mm²). For all measurements, very small excitation currents of 100 μ A were used in order to avoid Joule heating effects.²²

1. Etourneau, J.; Hagenmuller, P. Structure and physical features of the rare-earth borides. *Philos. Mag. B-Phys. Condens. Matter Stat. Mech. Electron. Opt. Magn. Prop.* **52**, 589-610 (1985).
2. Kasuya, T.; Kojima, K.; Kasaya, M. In *Valence Instabilities and Related Narrow-Band Phenomena*; Parks, R. D., Ed.; Springer US: 137 (1977).
3. Nickerson; J. C.; White, R. M.; Lee, K. N.; Bachmann, R.; Geballe, T. H.; Hull, G. W. Physical properties of SmB₆. *Phys. Rev. B: Condens. Matter* **3**, 2030-2042 (1971).
4. Dzero, M.; Sun, K.; Galitski, V.; Coleman, P. Topological Kondo insulators. *Phys. Rev. Lett.* **104**, 106408 (2010).
5. Takimoto, T. SmB₆: A promising candidate for a topological insulator. *J. Phys. Soc. Jpn.* **80**, 123710 (2011).
6. Dzero, M.; Sun, K.; Dzero, P.; Galitski, V. Theory of topological Kondo insulators. *Phys. Rev. B: Condens. Matter* **85**, 045130 (2012).
7. Alexandrov, V.; Dzero, M.; Coleman, P. Cubic topological Kondo insulators. *Phys. Rev. Lett.* **111**, 226403 (2013).
8. Kim, D. J. et al. Surface hall effect and nonlocal transport in SmB₆: evidence for surface conduction. *Sci. Rep.* **3**, 3150 (2013).
9. Neupane, M. et al. Surface electronic structure of the topological Kondo-insulator candidate correlated electron system SmB₆. *Nat. Commun.* **4**, 3991 (2013).
10. Wolgast, S. et al. Low-temperature surface conduction in the Kondo insulator SmB₆. *Phys. Rev. B: Condens. Matter* **88**, 180405 (2013).

11. Kim, D. J.; Xia, J.; Fisk, Z. Topological surface state in the Kondo insulator samarium hexaboride. *Nat. Mater.* **13**, 466 (2014).
12. Rößler, S. et al. Hybridization gap and Fano resonance in SmB₆. *Proc. Natl. Acad. Sci. U.S.A.* **111**, 4798-4802 (2014).
13. Thomas, S. et al. Weak antilocalization and linear magnetoresistance in the surface state of SmB₆. *arXiv:1307.4133*. (2013).
14. Suga, S. et al. Spin-polarized angle-resolved photoelectron spectroscopy of the so-predicted Kondo topological insulator SmB₆. *J. Phys. Soc. Jpn.* **83**, 014705 (2014).
15. Jiang, J. et al. Observation of possible topological in-gap surface states in the Kondo insulator SmB₆ by photoemission. *Nat. Commun.* **4**, 3010 (2013).
16. Zhu, Z. H. et al. A. Polarity-driven surface metallicity in SmB₆. *Phys. Rev. Lett.* **111**, 216402 (2013).
17. Denlinger, J. D. et al. SmB₆ photoemission: past and present. *arXiv:1312.6636v2*. (2014).
18. Xu, N. et al. Surface and bulk electronic structure of the strongly correlated system SmB₆ and implications for a topological Kondo insulator *Phys. Rev. B: Condens. Matter* **88**, 121102 (2013).
19. Frantzeskakis, E. et al. Kondo hybridization and the origin of metallic states at the (001) surface of SmB₆. *Phys. Rev. X* **3**, 041024 (2013).
20. Yee, M. et al. Imaging the Kondo Insulating Gap on SmB₆. *arXiv:1308.1085*. (2013).
21. Li, G. et al. Two-dimensional Fermi surfaces in Kondo insulator SmB₆. *Science* **346**, 1208-1212 (2014).
22. Phelan, W. A. et al. Correlation between Bulk Thermodynamic Measurements and the Low-Temperature-Resistance Plateau in SmB₆. *Phys. Rev. X* **4**, 031012 (2014).
23. Fuhrman, W. T. et al. Interaction driven subgap spin exciton in the Kondo insulator SmB₆. *Phys. Rev. Lett.* **114**, 036401 (2015).
24. Kebede, A. et al. Studies of the correlated electron system SmB₆. *Physica B* **223-24**, 256-259 (1996).

25. Gabani, S. et. al. Properties of the in-gap states in SmB₆. *Solid State Commun.* **117**, 641-644 (2001).
26. Koohpayeh, S. M.; Fort, D.; Abell, J. S. The optical floating zone technique: a review of experimental procedures with special reference to oxides. *Prog. Cryst. Growth Charact. Mater.* **54**, 121-137 (2008).
27. Syers, P.; Kim, D.; Fuhrer, M. S.; Paglione, J. Tuning bulk and surface conduction in the proposed topological Kondo insulator SmB₆. *Phys. Rev. Lett.* **114**, 096601 (2015).
28. Liao, P. K.; Spear, K. E.; Schlesinger, M. E. The B-Sm (boron-samarium) system. *J. Phase Equilib.* **17**, 347-350 (1996).
29. Tarascon, J. M. et. al. Temperature-dependence of the samarium oxidation-state in SmB₆ and Sm_{1-x}La_xB₆. *Physique* **41**, 1141-1145 (1980).
30. Paderno, Y. B.; Lundstrom, T. On the homogeneity ranges of LaB₆, EuB₆, and SmB₆. *Acta Chem. Scand. A* **37**, 609-612 (1983).
31. Yong, J. et. al. Robust topological surface state in Kondo insulator SmB₆ thin films. *Appl. Phys. Lett.* **105**, 222403 (2014).
32. Konrad, T.; Jeitschko, W.; Danebrock, M. E.; Evers, C. B. H. Preparation, properties and crystal structures of the thorium chromium borides ThCrB₄ and ThCr₂B₆; structure refinements of CeCr₂B₆, ThB₄ and ThB₆. *J. Alloys Compd.* **234**, 56-61 (1996).
33. Schmitt, K.; Stuckl, C.; Ripplinger, H.; Albert, B. Crystal and electronic structure of BaB₆ in comparison with CaB₆ and molecular [B₆H₆]²⁻. *Solid State Sci.* **3**, 321-327 (2001).
34. Ott, H. R. et. al. Structure and low temperature properties of SrB₆. *Phys. B* **102**, 337-335 (1997).
35. Blomberg, M. K.; Merisalo, M. J.; Korsukova, M. M.; Gurin, V. N. Single-crystal x-ray-diffraction study of NdB₆, EuB₆, and YbB₆. *J. Alloys Compd.* **217**, 123-127 (1995).
36. Ning, G. R.; Flemming, R. L. Rietveld refinement of LaB₆: data from μ XRD. *J. Appl. Cryst.* **38**, 757-759 (2005).

37. Mizumaki, M.; Tsutsui, S.; Iga, F. Temperature dependence of Sm valence in SmB₆ studied by x-ray absorption spectroscopy. *J. Phys. Conf. Ser.* **176**, 012034 (2009).
38. Dianoux, A. J.; Lander, G. H.; Institut Max von Laue, P. L. G.; Laue-Langevin, I. *Neutron Data Booklet*; Old City, (2001).
39. Wang, J. et. al. A dedicated powder diffraction beamline at the Advanced Photon Source: commissioning and early operational results. *Rev. Sci. Instrum.* **79**, 085105 (2008).
40. Larson, A. C.; Von Dreele, R. B. *Los Alamos National Laboratory Report LAUR 86-748*, Los Alamos National Laboratory: Los Alamos, NM (1995-2004).
41. Toby, B. H. EXPGUI, a graphical user interface for GSAS. *J. Appl. Crystallogr.* **34**, 210-213 (2001).
42. Altomare, A. et. al. SIR97: a new tool for crystal structure determination and refinement. *J. Appl. Crystallogr.* **32**, 115-119 (1999).
43. Sheldrick, G. M. A short history of SHELX. *Acta Crystallogr., Sect. A: Found. Crystallogr.* **64**, 112-122 (2008).
44. Clark, R. C.; Reid, J. S. The analytical calculation of absorption in multifaceted crystals. *Acta Cryst.* **51**, 887-897 (1995).
45. Zikovsky, J.; Peterson, P. F.; Wang, X. P.; Frost, M.; Hoffmann, C. CrystalPlan: an experiment-planning tool for crystallography. *J. Appl. Crystallogr.* **44**, 418-423 (2011).
46. Schultz, A. J. et. al. Integration of neutron time-of-flight single-crystal Bragg peaks in reciprocal space. *J. Appl. Crystallogr.* **47**, 915-921 (2014).
47. Schultz, A. J.; Srinivasan, K.; Teller, R. G.; Williams, J. M.; Lukehart, C. M. Single-crystal, time-of-flight, neutron-diffraction structure of hydrogen cis-diacetyltetracarbonylrhenate, [cis-(OC)₄Re(CH₃CO)₂]H: a metallaacetylacetonone molecule. *J. Am. Chem. Soc.* **106**, 999-1003 (1984).

Acknowledgments

The work at the Institute for Quantum Matter (IQM) was supported by the U.S. Department of Energy, Office of Basic Energy Sciences, Division of Materials Sciences and Engineering under Grant No. DE-FG02-08ER46544. Use of the Advanced Photon Source at Argonne National Laboratory was supported by the U. S. Department of Energy, Office of Science, Office of Basic Energy Sciences, under Contract No. DE-AC02-06CH11357. The neutron diffraction data were collected at the Oak Ridge National Laboratory's Spallation Neutron Source; supported by the Division of Scientific User Facilities, Office of Basic Energy Sciences, U.S. Department of Energy, under contract DE-AC05 00OR22725 with UT Battelle, LLC. W.A.P would like to thank Collin L. Broholm for helping in the procurement of the flux grown SmB_6 crystal.

Table 1. Crystallographic parameters for the floating zone cuts of SmB₆ obtained from Rietveld refinements to the 11-BM data. The Sm and B atoms reside on the *Ia* (0,0,0) and *6f* (*x*, 1/2, 1/2) Wyckoff position, respectively. The statistical uncertainties are given in parentheses.

	Cut 1	Cut 2	Cut 3	Cut 4
<i>T</i> (K)	295	295	295	295
Space group	<i>Pm-3m</i>	<i>Pm-3m</i>	<i>Pm-3m</i>	<i>Pm-3m</i>
<i>a</i> (Å)	4.134309(2)	4.133938(1)	4.133288(1)	4.133343(1)
<i>V</i> (Å ³)	70.67(1)	70.65(1)	70.61(1)	70.62(1)
<i>Z</i>	1	1	1	1
<i>x</i> position (B)	0.19985(18)	0.19855(16)	0.19962(15)	0.19997(1)
<i>U</i> _{Sm} (Å ²)	0.007763(20)	0.00802(2)	0.007428(16)	0.007360(12)
<i>U</i> _B (Å ²)	0.00258(13)	0.00266(12)	0.00177(11)	0.00230(12)
^a <i>R</i> _{<i>p</i>}	0.061	0.056	0.052	0.052
^b <i>R</i> _{<i>wp</i>}	0.080	0.073	0.067	0.072
^c <i>R</i> _{<i>exp</i>}	0.043	0.048	0.048	0.041
^d <i>χ</i>	3.386	2.280	1.904	3.098

$$^a R_p = \sum |Y_o - Y_C| / \sum Y_o; \quad ^b R_{wp} = [M / \sum w(Y_o^2)]^{1/2}; \quad ^c R_{exp} = R_{wp} / (\chi^2)^{1/2}; \quad ^d \chi = (M / N_{obs} - N_{va})^{1/2}$$

Table 2. Crystallographic parameters for the flux grown $^{154}\text{Sm}^{11}\text{B}_6$ crystal obtained from model fits to the TOPAZ neutron data. The statistical uncertainties are given in parentheses.

Temperature (K)	90	295
Space group	<i>Pm-3m</i>	<i>Pm-3m</i>
a (Å)	4.1306(2)	4.1319(2)
V (Å ³)	70.48(1)	70.54(1)
Z	1	1
Collected Reflections	977	1149
Crystal Size (mm ³)	$1.05 \times 1.10 \times 1.55$	$1.05 \times 1.10 \times 1.55$
$Goof$	1.30	1.13
$R_I[F^2 > 2\sigma(F^2)]^a$	0.060	0.067
$wR_2(F^2)^b$	0.166	0.190
$\Delta\rho_{\max}$ (fm Å ⁻³)	0.99	1.17
$\Delta\rho_{\min}$ (fm Å ⁻³)	-2.59	-3.21

$$^a R_I(F) = \sum ||F_o| - |F_c|| / \sum |F_o|; \quad ^b wR_2(F^2) = [\sum [w (F_o^2 - F_c^2)^2] / \sum [w (F_o^2)^2]]^{1/2}$$

Table 3. Atomic fractional coordinates, site occupancies, and ADPs for the flux grown $^{154}\text{Sm}^{11}\text{B}_6$ crystal obtained from model fits to the TOPAZ neutron data. The statistical uncertainties are given in parentheses.

$T = 90$ K

atom	Wyckoff Site	x	y	z	Occupancy	$U_{11}(\text{\AA}^2)$	$U_{22}(\text{\AA}^2)$	$U_{33}(\text{\AA}^2)$
Sm1	$1a$	0	0	0	1	0.00254(18)	0.00254(18)	0.00254(18)
B1	$6f$	0.19984(7)	$\frac{1}{2}$	$\frac{1}{2}$	1	0.00230(18)	0.00361(18)	0.00361(18)

$T = 295$ K

atom	Wyckoff Site	x	y	z	Occupancy	$U_{11}(\text{\AA}^2)$	$U_{22}(\text{\AA}^2)$	$U_{33}(\text{\AA}^2)$
Sm1	$1a$	0	0	0	1	0.0066(2)	0.0066(2)	0.0066(2)
B1	$6f$	0.19964(6)	$\frac{1}{2}$	$\frac{1}{2}$	1	0.00267(19)	0.0044(2)	0.0044(2)

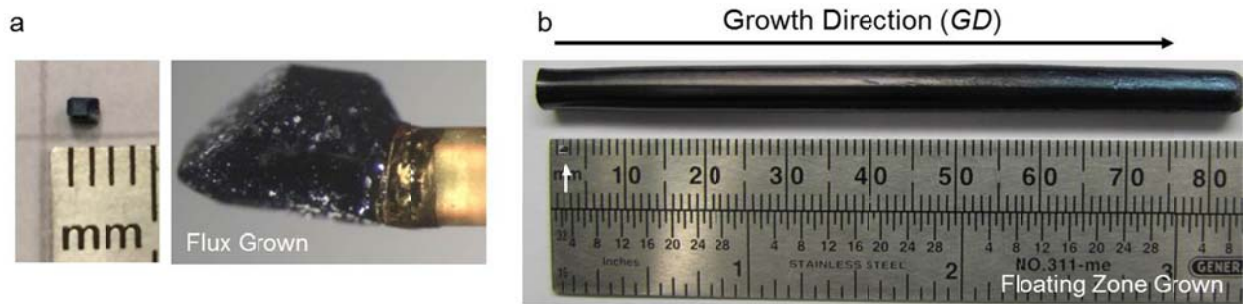


Figure 1. a) Pictures of a flux grown single crystal (right) and as mounted onto a Kapton covered vanadium post used for neutron diffraction measurements. b) A single crystal prepared *via* the floating zone procedure. Also shown is a scaled version of the picture of the flux grown single crystal (white arrow).

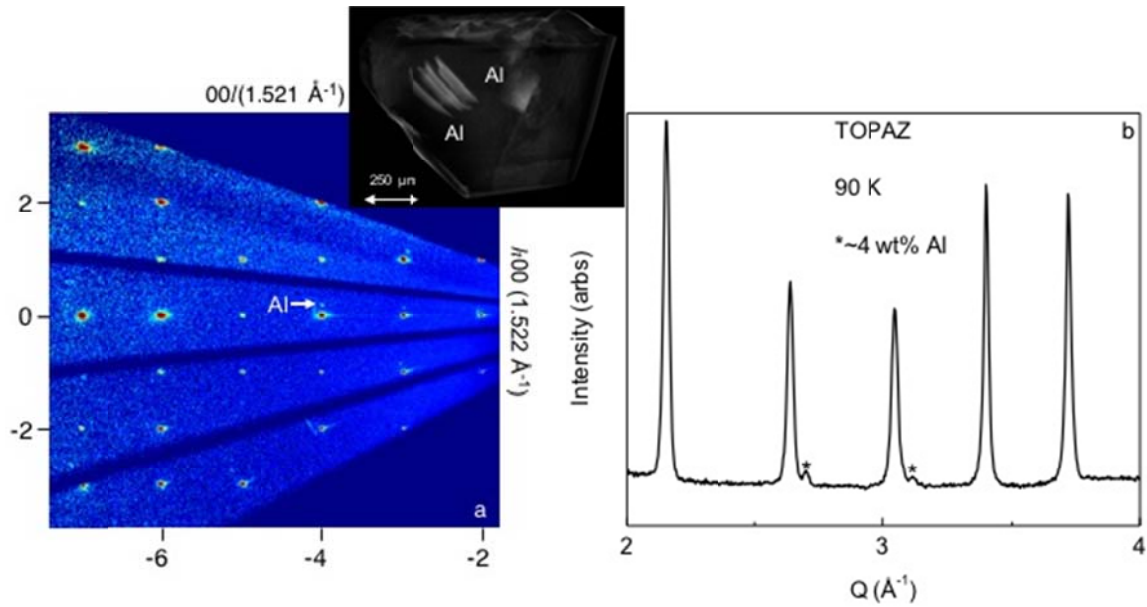


Figure 2. a) A $00l$ versus $h00$ precession image of the $^{154}\text{Sm}^{11}\text{B}_6$ flux grown crystal collected at $T = 90$ K using the TOPAZ single crystal diffractometer located at the Spallation Neutron Source and a X-ray CT image showing the presence of inclusions within the $^{154}\text{Sm}^{11}\text{B}_6$ crystal. The companion reflections (see white arrow) correspond to epitaxial aluminum present in this flux grown crystal, determined using b) a neutron diffraction histogram obtained from radial integration of the single crystal neutron diffraction data. The asterisks denote the reflections from the epitaxial aluminum present in the flux grown crystal of SmB_6 .

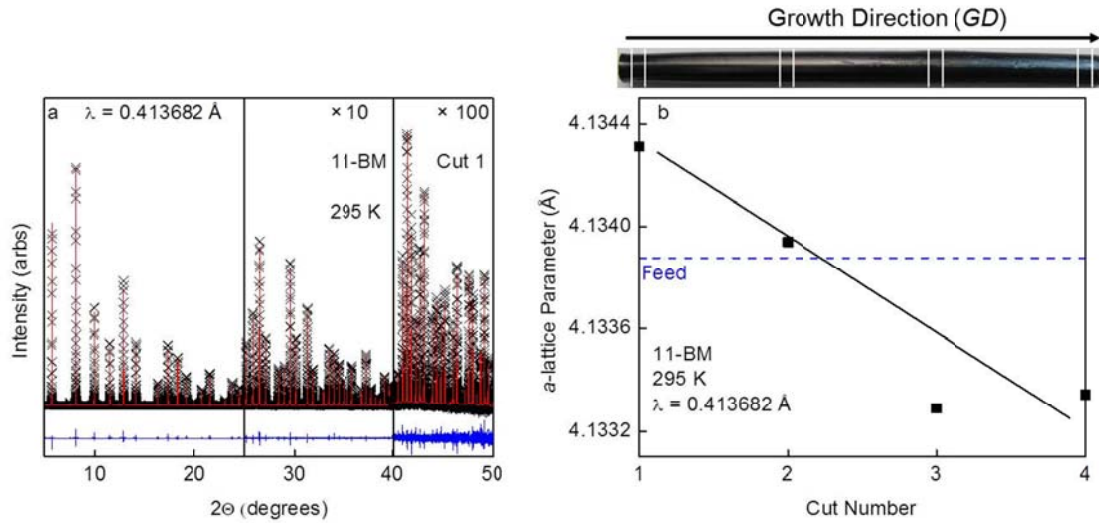


Figure 3. a) Rietveld refinement to synchrotron X-ray diffraction data at $T = 295$ K collected on Cut 1 of the SmB_6 floating zone grown single crystal. The black crosses, red lines, and blue lines correspond to the collected data, refined model, and difference curve respectively. The higher angle data are multiplied by $\times 10$ ($25 \geq 2\theta \geq 40$) and $\times 100$ ($40 \geq 2\theta \geq 50$) to highlight the quality of the fit. Fits to cuts 2-4 are of similar quality. b) The refined a -lattice parameter values for cuts 1-4 versus cut number, where this value decreases with cut number. The line serves as a guide to the eye and the error bars are contained within the data points. Additionally, the refined a -lattice parameter value for the polycrystalline feed rod used for the growth of the FZ SmB_6 crystal versus cut number (blue dashed line) is shown.

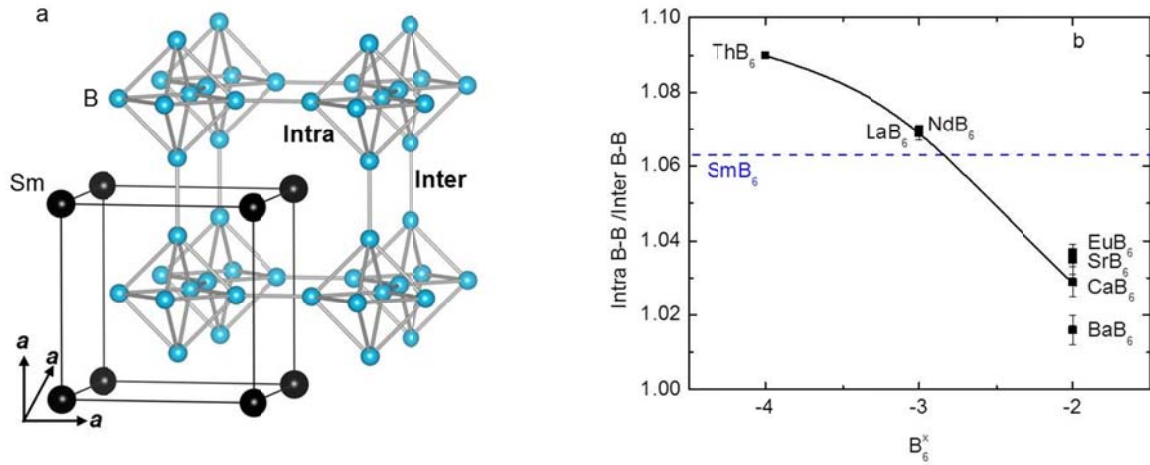


Figure 4. a) Structural depiction of SmB₆. b) The intra boron-boron bond distances normalized by the inter boron-boron distances (Intra B-B/Inter B-B) of the B₆ octahedral cluster for selected hexaborides versus different charges of the B₆ cluster (B₆^x) (■). Also shown is the Intra B-B/Inter B-B for all SmB₆ *FZ* cuts and the *FG* SmB₆ sample (blue dashed line). The charge on the B₆ cluster for SmB₆ mostly closely resembles -3, but is slight reduced, consistent with a partial mixed valency. The curved solid line serves as a guide to the eye.

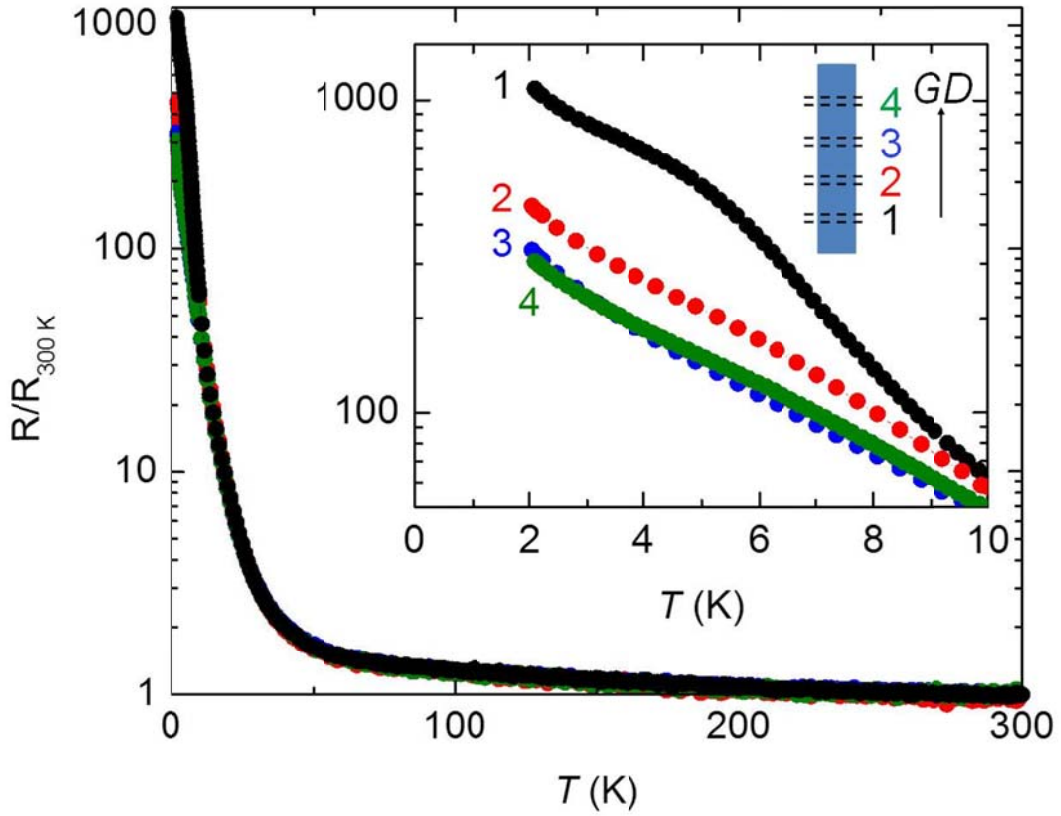


Figure 5. Resistance (R) normalized by the room temperature resistance values ($R_{300\text{ K}}$) versus temperature (T) for cuts 1-4. The inset highlights the trend in normalized resistance from 0 to 10 K showing that the magnitude of $R/R_{300\text{ K}}$ and the degree of plateauing decreases from 1 to 4.

Supporting Information For: On the Chemistry and Physical Properties of Flux and Floating Zone Grown SmB₆ Single Crystals

W. A. Phelan,^{1,2,3*} S. M. Koohpayeh,² P. Cottingham,^{1,2,3} J. A. Tutmaher,^{1,2,3} J. C. Leiner,⁴ M. D. Lumsden,⁴ C. M. Lavelle,⁵ X. P. Wang,⁶ C. Hoffmann,⁶ M. A. Siegler,¹ and T. M. McQueen^{1,2,3*}

¹*Department of Chemistry, Johns Hopkins University, Baltimore, MD 21218, USA*

²*Institute for Quantum Matter, Department of Physics and Astronomy, Johns Hopkins University, Baltimore, MD 21218, USA*

³*Department of Materials Science and Engineering, Johns Hopkins University, Baltimore, MD 21218, USA*

⁴*Quantum Condensed Matter Division, Oak Ridge National Laboratory, Oak Ridge, TN 37831, USA*

⁵*Applied Nuclear Physics Group, Johns Hopkins University, Applied Physics Laboratory, Laurel, MD, 20723, USA*

⁶*Chemical and Engineering Materials Division, Neutron Sciences Directorate, Oak Ridge National Laboratory, Oak Ridge, TN 37831, USA*

*wphelan2@pha.jhu.edu and mcqueen@jhu.edu

Figure S1. A movie showing the reconstructed X-ray computed tomography (CT) frames of the $^{154}\text{Sm}^{11}\text{B}_6$ flux-grown crystal [photo only on arXiv]. It is obvious that this crystal is composed of two materials, one with a high atomic number (dark contrast) and low Z low atomic number (light contrast).

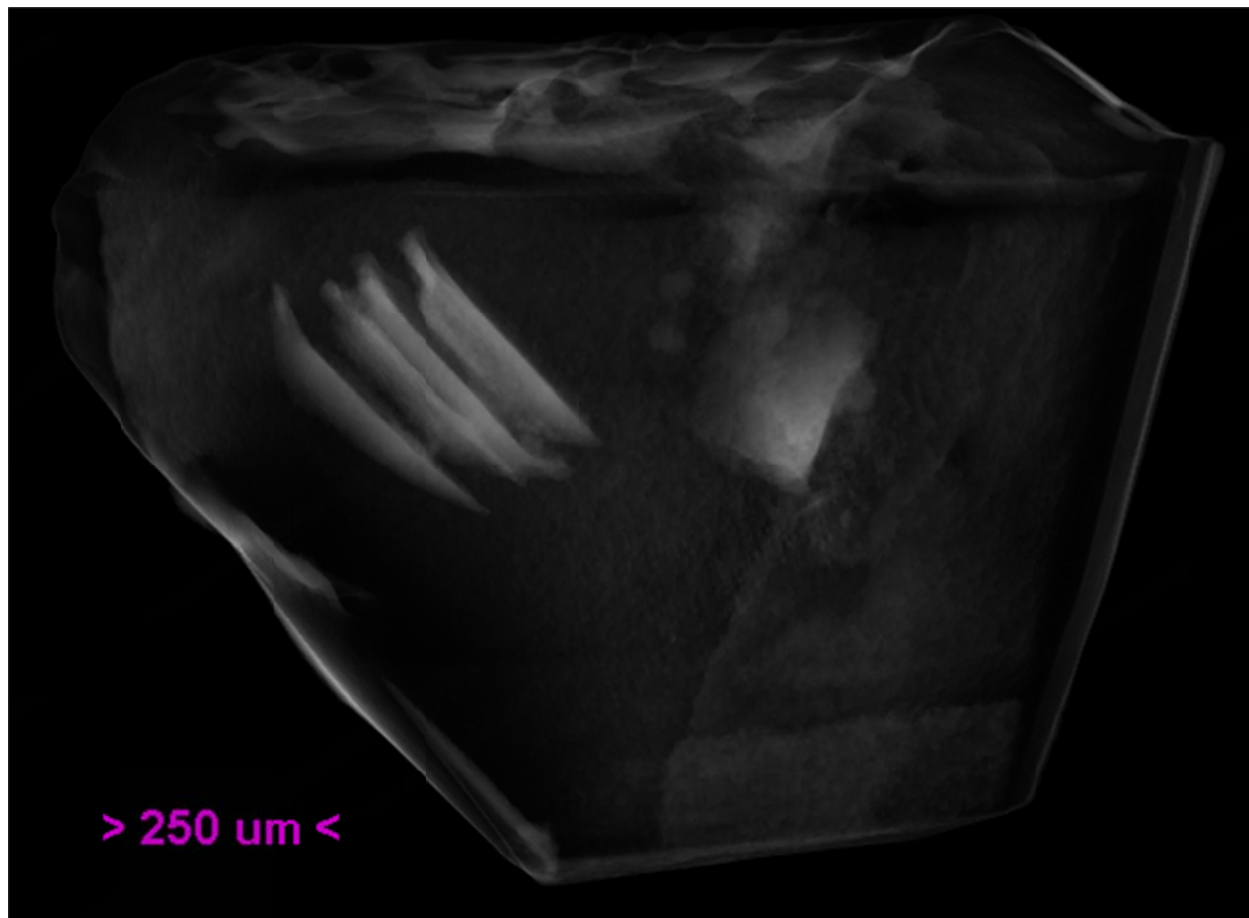


Figure S2. Rietveld refinements to synchrotron X-ray diffraction data at $T = 295$ K collected on a) cut 2 b) cut 3, and c) cut 4 of the SmB_6 floating zone grown single crystal. The black crosses, red lines, and blue lines correspond to the collected data, refined model, and difference curve respectively. The higher angle data are multiplied by $\times 10$ ($25 \geq 2\Theta \geq 40$) and $\times 100$ ($40 \geq 2\Theta \geq 50$) to highlight the quality of the fit.

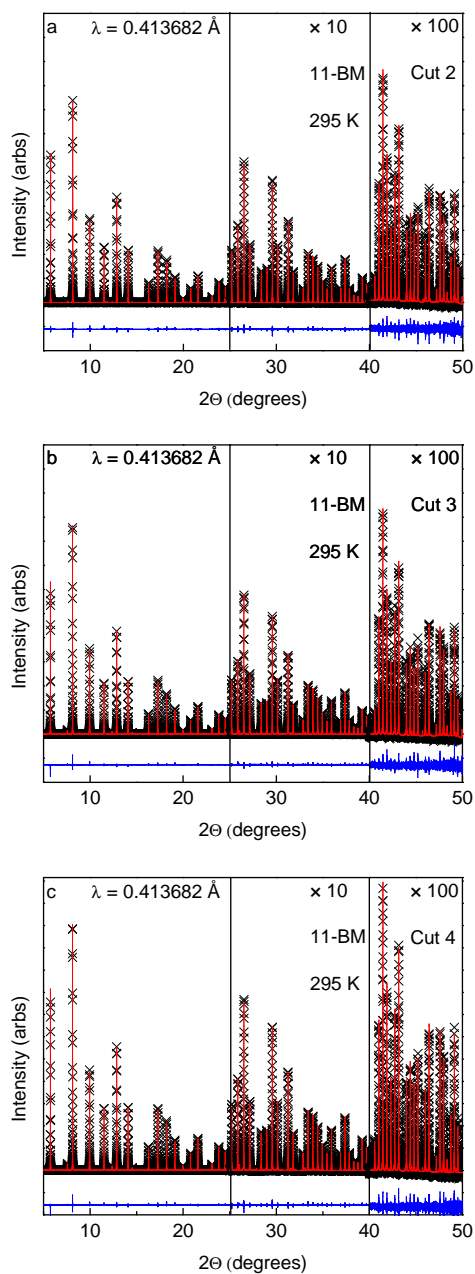


Figure S3. Rietveld refinements to X-ray diffraction data at $T = 295$ K collected on the vaporized material, which amounted only to approximately 1% of the total material from the SmB_6 floating zone single crystal growth. The black crosses, red lines, and blue lines correspond to the collected data, refined model, and difference curve respectively. It is obvious from fits to this data that this vaporized material is a multi-phase mixture of SmB_6 (gray ticks) and SmB_4 (orange ticks).

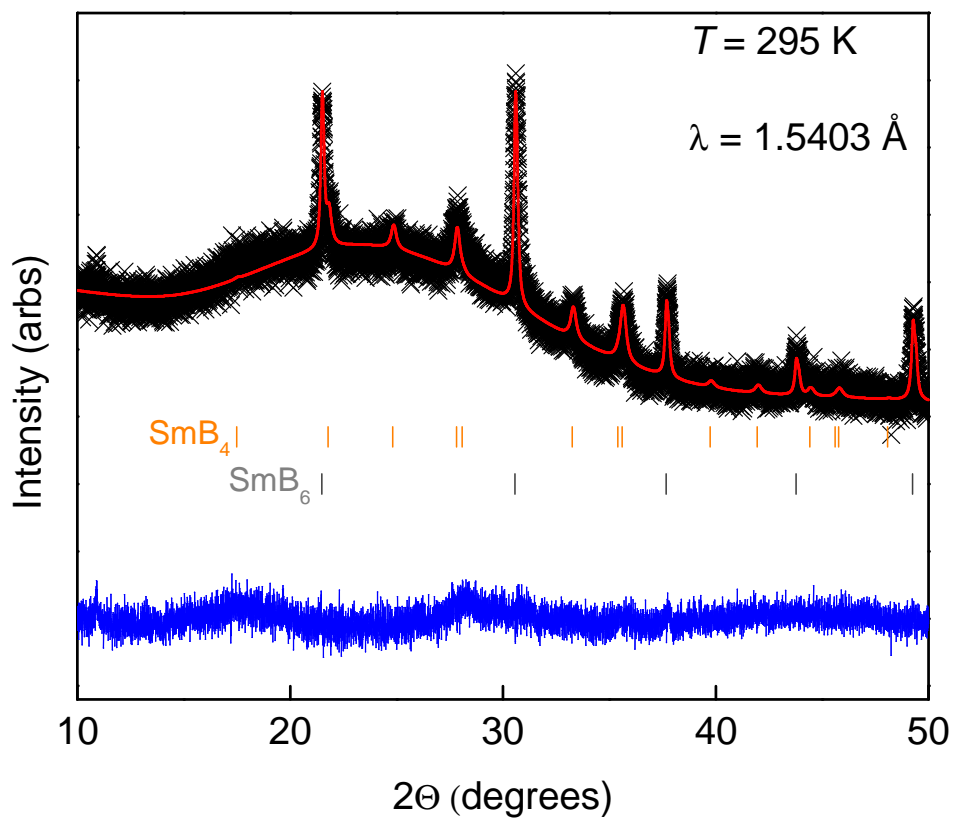


Figure S4. The (110), (310), and (640) reflections for cuts 1-4 where the peak positions were normalized along the x-axis relative to a silicon standard. All peak positions reside at higher angles when going from cuts 1 to 3 for each reflection, showing that the lattice parameters decrease with compositional variations along the crystal. The overlapping of the (110), (310), and (640) peak positions for cuts 3 and 4 show that these cuts have roughly the same lattice parameters and compositions.

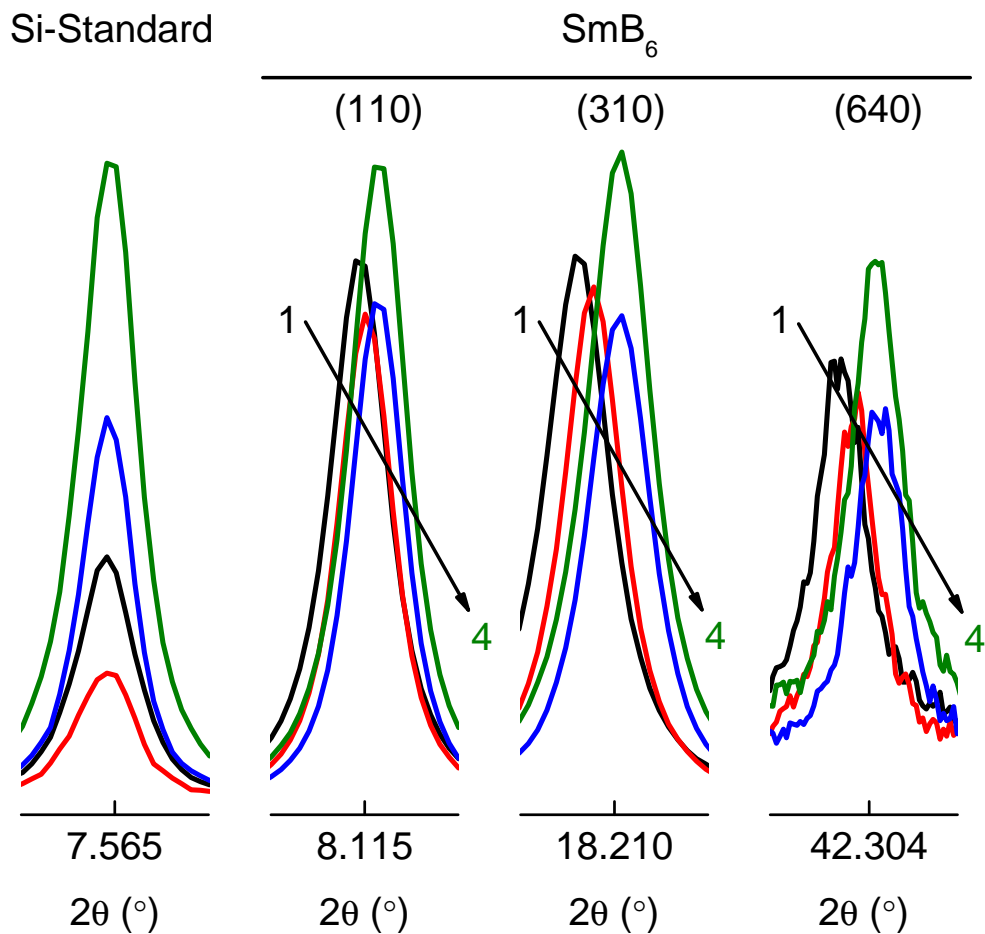


Figure S5. A plot of the resistance (R) normalized by the room temperature resistance values ($R_{300\text{ K}}$) versus temperature (T) for cuts 1'-3' (open circles) and cuts 1-3 (closed circles, Figure 5) from 0 to 10 K. To check the reproducibility of our resistance measurements, the authors removed the original platinum leads used to collect the data presented in Figure 5 for cuts 1-3, polished these three cuts, mounted new leads, and recollected the data (cuts 1'-3'). Additionally, resistances were measured using a new cut between the location of the original cut 1 and cut 2 (cut 2'') and a new cut beyond the location of the original cut 4 (cut 4''). Very much like the data for cuts 1-4 in Figure 5, the magnitude of the $R/R_{300\text{ K}}$ and the degree of plateauing decrease and the cut number gets larger for all cuts. Finally, the trend in lattice parameters of 4.1333(4) Å and 4.13284(3) Å for cut 2'' and cut 4'', respectively, agrees well with the resistance and lattice parameter trend for the original cuts 1- 4.

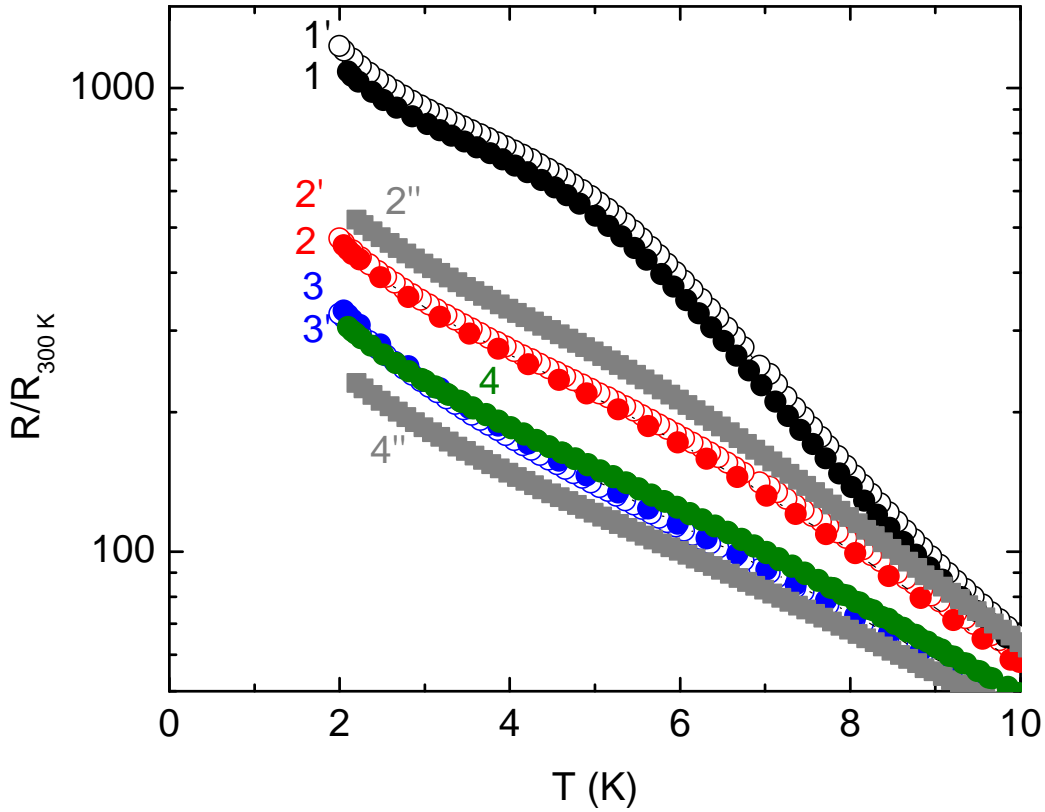


Figure S6. Concentration (ppm wt) of elements present in the starting material and cuts 1-3 versus Atomic Number. These semi-quantitative trace elemental analyses results were obtained from glow discharge mass spectrometry (GDMS) experiments and are tabulated in Table S5.

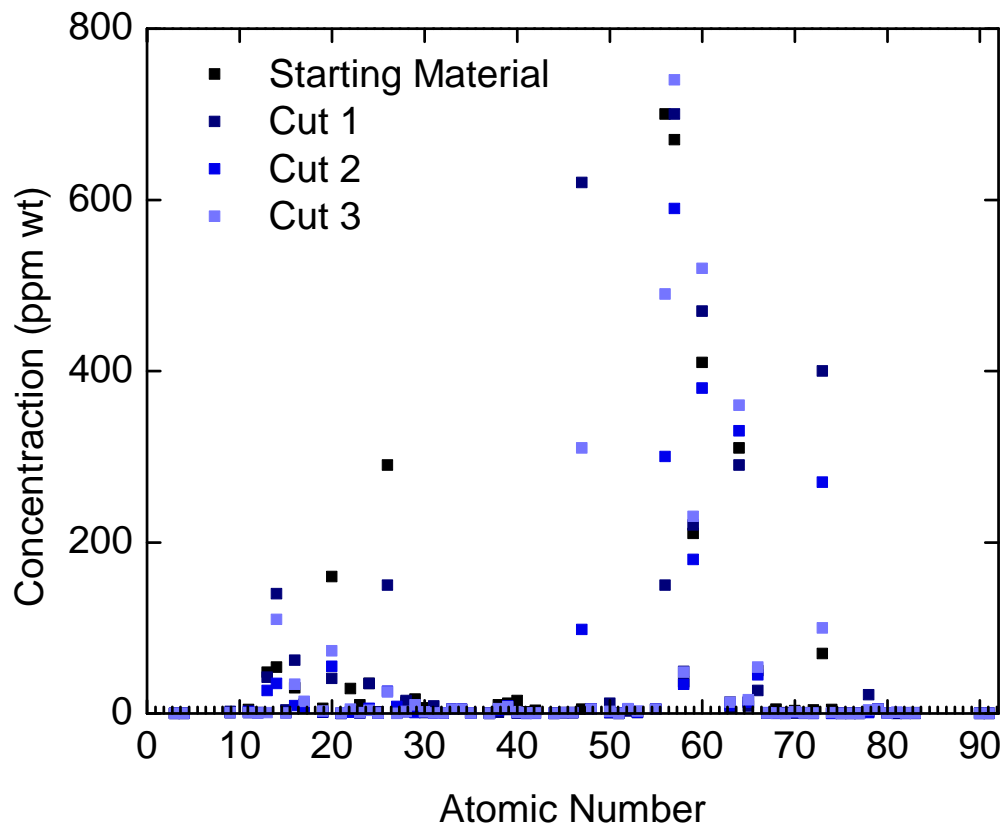


Table S1. Crystallographic parameters for the flux grown $^{154}\text{Sm}^{11}\text{B}_6$ crystal obtained from model fits to the single crystal X-ray diffraction data. The statistical uncertainties are given in parentheses.

Temperature (K)	293(2)
Composition	$\text{SmB}_{5.88}$
Space group	$Pm-3m$
a (Å)	4.13283(2)
V (Å ³)	70.590(1)
Z	1
Collected Reflections	7089
Independent Reflections	154
$Goof$	1.18
$R_I[F^2 > 2\sigma(F^2)]^a$	0.009
$wR_2(F^2)^b$	0.020
$\Delta\rho_{\max}$ (e Å ⁻³)	1.00
$\Delta\rho_{\min}$ (e Å ⁻³)	-1.36

$$^a R_I(F) = \sum ||F_o| - |F_c|| / \sum |F_o|; \quad ^b wR_2(F^2) = [\sum [w (F_o^2 - F_c^2)^2] / \sum [w (F_o^2)^2]]^{1/2}$$

Table S2. Atomic fractional coordinates, site occupancies, and ADPs for flux grown $^{154}\text{Sm}^{11}\text{B}_6$ crystal obtained from model fits to the single crystal X-ray diffraction data. The statistical uncertainties are given in parentheses.

$T = 293(2)$ K

atom	Wyckoff Site	x	y	z	Occupancy	$U_{11}(\text{\AA}^2)$	$U_{22}(\text{\AA}^2)$	$U_{33}(\text{\AA}^2)$
Sm1	<i>1a</i>	0	0	0	1	0.00776(4)	0.00776(4)	0.00776(4)
B1	<i>6f</i>	0.2000(1)	$\frac{1}{2}$	$\frac{1}{2}$	0.98	0.0036(2)	0.0036(2)	0.00523(14)

Table S3. The percent abundance for the differing isotopes of boron and samarium in the flux grown doubly enriched $^{154}\text{Sm}^{11}\text{B}_6$ crystal.

	<u>% Abundance of Boron</u>		<u>% Abundance of Samarium</u>						
	^{10}B	^{11}B	^{144}Sm	^{147}Sm	^{148}Sm	^{149}Sm	^{150}Sm	^{152}Sm	^{154}Sm
Doubly Enriched SmB_6 Crystal	3.6(1)	96.4(2.1)	0.0067(2)	0.044(1)	0.041(1)	0.0550(3)	0.0390(2)	0.305(2)	99.51(0.74)

Table S4. The concentration of differing elements present in the SmB₆ starting material, cut 1, cut 2, and cut3.

	Concentration (ppm wt)			
	Starting Material	Cut 1	Cut 2	Cut 3
Li	<0.05	<0.05	<0.05	<0.05
Be	<0.05	<0.05	<0.05	<0.05
B	Bulk	Bulk	Bulk	Bulk
F	<1	2.2	<1	<1
Na	4.7	0.97	2.4	0.83
Mg	0.95	1.1	0.91	0.47
Al	48	42	27	0.99
Si	54	140	35	110
P	0.78	4.3	1.1	0.52
S	30	62	9.1	34
Cl	~10	~11	~7	~14
K	6.1	1.3	1.8	2.6
Ca	160	41	55	73
Sc	0.06	0.08	<0.05	0.44
Ti	29	2.0	1.4	5.2
V	10	0.46	0.79	0.76
Cr	35	35	6.0	3.8
Mn	0.65	2.0	0.38	0.27
Fe	290	150	26	25
Co	0.64	2.4	8.2	0.19
Ni	13	15	1.9	2.1
Cu	17	4.3	0.81	9.8
Zn	6.5	0.72	1.9	1.8
Ga	<0.5	8.5	<0.5	<0.5
Ge	<0.5	<0.5	<0.5	<0.5
As	<5	<5	<5	<5
Se	<5	<5	<5	<5
Br	<0.5	<0.5	<0.5	<0.5
Rb	<0.05	<0.05	<0.05	<0.05

Table S4 continued. The concentration of differing elements present in the SmB₆ starting material, cut 1, cut 2, and cut3.

	Concentration (ppm wt)			
	Starting Material	Cut 1	Cut 2	Cut 3
Sr	10	1.5	3.8	5.5
Y	12	4.5	8.4	7.7
Zr	15	0.33	0.71	1.2
Nb	1.8	0.10	<0.05	0.29
Mo	3.8	0.45	<0.05	0.49
Ru	<0.05	0.16	<0.05	<0.05
Rh	<1	<1	<1	<1
Pd	<1	<1	<1	<1
Ag	5.2	620	98	310
Cd	<5	<5	<5	<5
In	Binder	Binder	Binder	Binder
Sn	<1	12	<1	2.3
Sb	<0.1	<0.1	<0.1	<0.1
Te	4.2	2.7	4.8	5.4
I	1.8	0.73	1.2	2.9
Cs	<5	<5	<5	<5
Ba	700	150	300	490
La	670	700	590	740
Ce	37	49	34	48
Pr	210	220	180	230
Nd	410	470	380	520
Sm	Bulk	Bulk	Bulk	Bulk
Eu	13	6.6	9.5	13
Gd	310	290	330	360
Tb	13	8.7	13	16
Dy	50	27	45	54
Ho	0.48	0.30	1.1	0.44
Er	5.1	0.15	0.35	0.61
Tm	0.95	<0.05	<0.05	0.11

Table S4 continued. The concentration of differing elements present in the SmB₆ starting material, cut 1, cut 2, and cut3.

	Concentration (ppm wt)			
	Starting Material	Cut 1	Cut 2	Cut 3
Yb	3.2	0.35	1.5	1.7
Lu	0.94	0.08	0.25	0.51
Hf	4.1	<0.1	<0.1	0.63
Ta	≤70	≤400	≤270	≤100
W	4.7	<0.1	<0.1	1.0
Re	<0.1	<0.1	<0.1	<0.1
Os	<0.1	<0.1	<0.1	<0.1
Ir	<0.1	<0.1	<0.1	0.19
Pt	1.8	22	1.1	3.9
Au	<5	<5	<5	<5
Hg	<0.5	<0.5	<0.5	<0.5
Tl	<0.01	0.10	0.93	1.5
Pb	<0.05	1.1	0.11	0.28
Bi	<0.05	1.1	0.11	0.24
Th	0.04	0.03	0.04	0.07
U	0.03	0.01	0.02	0.03
